DE GRUYTER OPEN

***MINERALOGIA**, 45, No 3-4: 99-120 (2014)*
DOI: 10.1515/mipo-2015-0007
www.Mineralogia.pl

MINERALOGICAL SOCIETY OF POLAND
POLSKIE TOWARZYSTWO MINERALOGICZNE

Original paper

Printed in 2015

Petrogenesis of kyanite-quartz segregations in mica schists of the Western Tatra Mountains (Slovakia)

Paulina PYKA[1]*, Aleksandra GAWĘDA[1], Krzysztof SZOPA[1], Axel MÜLLER[2], Magdalena SIKORSKA[3]

[1]*University of Silesia, Faculty of Earth Sciences, ul. Będzińska 60, 41-200 Sonowiec, Poland*
[2]*Geological Survey of Norway (NGU), Leiv Eirikssons vei 39, 7040 Trondheim, Norway*
[3]*Polish Geological Institute, Rakowiecka 4, Warsaw, Poland*
**Corresponding author e-mail: paulina.pyka@vp.pl*

Received: March 3, 2015
Received in revised form: September 15, 2015
Accepted: September 17, 2015
Available online: October 10, 2015

Abstract. In the Tatra Mountains (Slovakia) metamorphic complex, kyanite-quartz segregations with biotite-rich selvage occur in mylonitized mica schists. In this paper, the problem of fluid flow and aluminium mobility during the uplift of the crystalline massif, and the position of the segregations in the history of Western Tatra metamorphic complex, is adressed. The reaction Alm + Rt → Ilm + Ky + Qtz is considered to be the result of a pressure drop from above to below 9 kbar. Ti-in-biotite geothermometry shows the temperature range to be 579-639ºC that is related to heating and decompression associated with granite intrusion. Major-element mass-balance calculations show that Al remained stable in the selvage + segregation system whereas other elements (e.g. Cr, HFSE) were mobilized. The kyanite-quartz segregations formed from local fluids generated during dehydration of the metapelitic rocks during uplift. The main mechanism was likely diffusion-driven mass-transfer into extension-related cracks.

Key-words: kyanite-quartz segregation, aluminium mobilization, mass-balance, Tatra Mountains

1. Introduction

Kyanite, one of the polymorphic varieties of Al_2SiO_5, is an excellent marker of medium- to high-pressure metamorphism in metasedimentary rocks. However, specific vein- and lens-shaped segregations of Al_2SiO_5 polymorphs with quartz occur in many places in

metapelitic rocks showing Barrowian metamorphism (Allaz et al. 2005; Ague 2011). Their presence is usually interpreted as due to SiO_2 and Al_2O_3 mobilization and crystallization from channelized fluid exsolved during metamorphism (Ague 2011). Kyanite segregations have also been described from eclogites and interpreted as a result of local segregation phenomena (Widmer, Thompson 2001; Moussallam et al. 2012). These segregations may reflect (a) external fluid infiltration with advection of dissolved material, (b) single-pass or multi-pass infiltration of external fluids recycled by convection, (c) deformation-enhanced addition of advective material from a local fluid and/or (d) diffusion through stagnant fluid steered by a chemical gradient between vein and enclosing rocks (Widmer, Thompson 2001 and references therein).

In the Tatra Mountains metamorphic complex, megacrystic kyanite-quartz segregations occur within the mylonitized mica-schists on the SW-slope of Baranèc Mt. in Slovakia (Pyka et al. 2013a, b). The aim of the current paper is to discuss the problem of fluid flow and aluminium mobility during the uplift of the crystalline massif and the position of the kyanite-quartz segregations in the history of the Western Tatra metamorphic complex.

2. Geological setting and sampling

The Tatra Mountains crystalline basement is one of several core-mountains showing Variscan consolidation among the Mesozoic and Cenozoic sedimentary rocks of the Alpine chain of the Carpathians (Fig. 1a). The predominant part of the Tatra Mountains is formed by a polygenic Variscan granitoid intrusion (Gawęda, Szopa 2011; Burda et al. 2011; Burda et al. 2013). The metamorphic envelope of the intrusion is preserved mostly in the western part of the massif − the Western Tatra Mountains (Fig. 1b) and locally, as xenolithes, inside the granitoid intrusion (Gawęda 2009). In the metamorphic envelope, crystalline nappes were formed as a result of the Variscan collision and metamorphism, and partial melting of the accretionary prism occurred. The nappes are built of rocks of different lithologies (metapelites-metapsammites and metabasalts) and differing metamorphic grade, divided by the local shear zones (Gawęda, Burda 2004; Burda, Gawęda 2009; Moussalam et al. 2012; Deditius 2004). Their presence is linked to the closure of the Rheic Ocean (Gawęda, Golonka 2011).

On Baranièc Mt., two metamorphic nappes (units) bordered by the so called Baranièc overthrust have been defined (Gorek 1956; Gorek 1969; Fig. 1b, 2). The Upper Unit shows the higher metamorphic grade whereas the Lower Unit is characterised by a lower metamorphic grade: together, they define an inverted metamorphic zonation (Kohút, Janak 1994; Moussalam et al. 2012). Similar field relations have been described from the northern part of the metamorphic complex where metamorphic conditions in the Upper Unit estimated at 670-780ºC and 7.5-9 kbar, resulted in partial melting and migmatization (Gawęda, Kozłowski 1998; Burda, Gawęda 2009). In the Lower Unit, composed of metapelites (gneisses and mica schists) representing a metaflysch sequence, metamorphic conditions have been estimated at 540-580ºC and 5-8 kbar (Gawęda, Kozłowski 1998).

Megacrystic kyanite crystals, from 3 to 12 cm long (Fig. 3a) and showing the typical blue colour, are the main components of lens-like in shape kyanite-quartz segregations < 20 cm thick. The segregtios are located in cracks and pressure shadows in the strongly mylonitized mica schists on the south-western slope of Baranèc Mt. (Pyka et al. 2013b).

The segregations were sampled (Ky1 and Ky2) from the slope above Holy Vrch, in the SE part of Baranèc Mt. (Fig. 2).

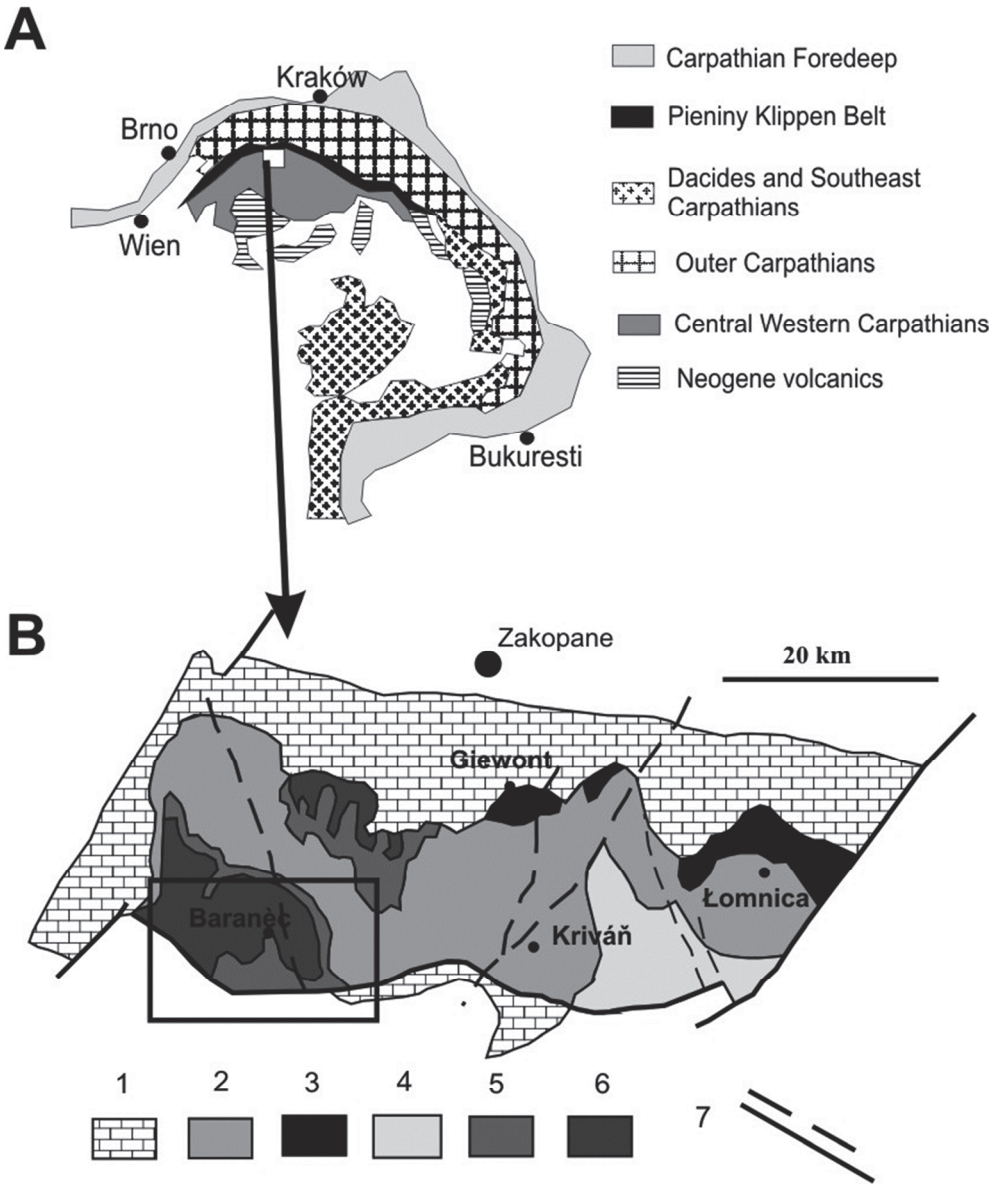

Fig. 1. General geological sketch of the Carpathian Belt (A) and a general geological map of the Tatra Mountains (B) - compilation from Gawęda (2009) and Moussalam et al. (2012).
1- Mesozoic sediments, 2 - common Tatra granite, 3 - Goryczkowa type granite, 4 - High Tatra type granite, 5 - metamorphic rocks of Upper Unit, 6 - metamorphic rocks of Lower Unit, 7- faults identified & assumed.

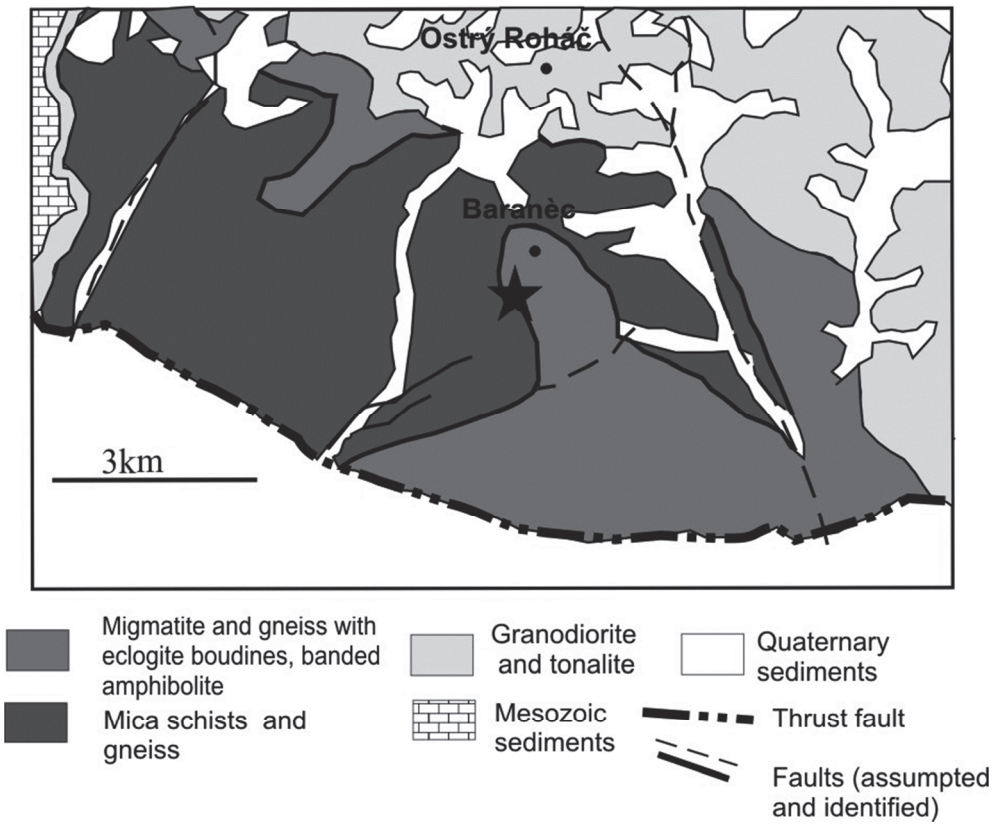

Fig. 2. General geological map of the study area (rectangle on Fig. 1). Star - sampling location. Map after Moussalam et al. (2012).

3. Analytical methods

Microscopic observations using an OLIMPUS BX-51 microscope (Faculty of Earth Sciences, University of Silesia) were followed by cathodoluminescence imaging using a CCL 8200 mk3 apparatus (Cambridge Image Technology Ltd.) mounted on an Optiphot 2 Nikon microscope (Polish Geological Institute, Warsaw). The applied accelerating voltage was 20 kV, the beam current 500 mA and the vacuum 0.5-0.2 Torr.

Electron probe micro analyses (EPMA) of major elements were done in the Inter-Institutional laboratory of Microanalyses of Minerals and Synthetic Substances, Warsaw, using a Cameca SX-100 electron microprobe. The analytical conditions were: acceleration voltage 15 kV, beam current 10 nA, counting time 4 s for peak and background, beam diameter 1-5 μm. Natural- and synthetic standards used were wollastonite for Si and Ca, orthoclase for Al and K, diopside for Mg, rhodonite for Mn and synthetic hematite for Fe. Trace elements were analysed by laser ablation inductively coupled plasma mass spectrometry (LA-ICP-MS) in the Geological Survey of Norway, Trondheim, using a double focusing sector field instrument (model-ELEMENT-1, Finnigan MAT) combined

with a New Wave UP-193 nm excimer laser probe. Continuous raster ablation was carried out using a repetition rate of 10 Hz, a spot size of 50 μm, a laser speed of 10 μm/s and pulse energy of 16.4 mJ. LA-ICP-MS was used for the in-situ determination of Na^{23}, Mg^{24}, K^{39}, Ca^{44}, Ti^{47}, V^{51}, Cr^{52}, Mn^{55} and Fe^{56} in the kyanite.

X-ray powder diffraction data of separated kyanite crystals were collected at the Faculty of Earth Sciences, University of Silesia, using a PW3040/60 diffractometer ($CoK_{\alpha 1}$ radiation, 45 kV, 30 mA, scan range 2.5-65°2Θ, step size 0.01°2Θ, scan step time 300 s). Structural data were obtained using XPERT High Score+ software and the standard data base ICDD PDF4+ 2012.

Bulk chemical compositions were analyzed by X-ray fluorescence (XRF; major elements and LILE), in combination with inductively coupled plasma-emission spectrometry and mass spectrometry (ICP-ES and ICP-MS; HFS elements) by ACME Analytical Laboratories, Vancouver, Canada. Preparation involved lithium borate fusion and dilute digestions or hot four-acid digestion for ICP-ES, $LiBO_2$ fusion for XRF and lithium borate decomposition or aqua regia digestion for ICP-MS. LOI was determined at 1000°C.

4. Results

4.1. Petrography and mineral chemistry

The kyanite-quartz segregations occur in mylonitized micaschists. The schists are composed of quartz, muscovite, biotite, garnet and plagioclase. Foliation is defined by the alignment of muscovite and biotite.

The segregations are composed of kyanite, quartz, fibrolitic silimanite and muscovite with accessory plagioclase, apatite with inclusions of garnet, biotite and rutile. The segregations are bordered by selvages of biotite, fibrolitic silimanite, feldspar, relict kyanite, accessory ilmenite, rutile and apatite. Chlorite and muscovite are secondary. Two mineral parageneses can be distinguished: (I) Rt-Grt_1-Ky-Bt_1 and (II) Ilm-Grt_2-Sil-Bt_2(-Ms).

4.1.1. Kyanite-quartz segregations

The main components of the segregations are isomorphic- to sub-idiomorphic bluish kyanite crystals (Fig. 3a) characterized by almost ideal crystal-chemical formulae with only small Fe substitutions (Table 1). The kyanite crystals are replaced by fibrolitic sillimanite that mantles kyanite aggregates (Fig. 3c, 4b). Thin sections reveal the presence of muscovite (Ms_1) replacing the kyanite and sillimanite, both from outer rims and along cleavages (Fig. 3c). Microchemical analyses indicate Tschermak substitution ($Al^{IV}Al^{VI} \leftrightarrow Si^{IV}Mg^{VI}$) in the muscovite ($Ms_1$) and Fe and Ti enrichment (0.112-0.442 a.p.f.u. Fe and < 0.102 a.p.f.u. Ti; Table 2). Xenomorphic quartz shows undulose extinction. Accessory plagioclase (oligoclase-albite) is represented by subhedral, normally zoned crystals ($Ab_{86}An_{11}Or_3$ - $Ab_{78}An_{21}Or_1$ in cores to $Ab_{99}Or_1$ - $Ab_{97}Or_3$ at rims) up to 200 μm in size. Inclusions of apatite-(Ca,F), < 300 μm in size occur in kyanite; in both apatite and host kyanite, inclusions of idiomorphic garnet, biotite and rutile are found (< 10 μm in size; Fig.

4a, 5a, b). Garnet (Grt_1) is almandine-spessartine ($Alm_{63}Spes_{18}Py_6Gros_{10}Andr_3$ - $Alm_{68}Spes_{16}Py_8Gros_5Andr_3$; Table 3). Biotite ($Bt_1$) is characterized by Fe/(Fe + Mg + Mn), i.e. *#fm* in the range of 0.544-0.553 and Ti = 0.215-0.232 a.p.f.u. (Table 4). Rutile inclusions (< 50 μm) are usually idiomorphic (Fig. 5).

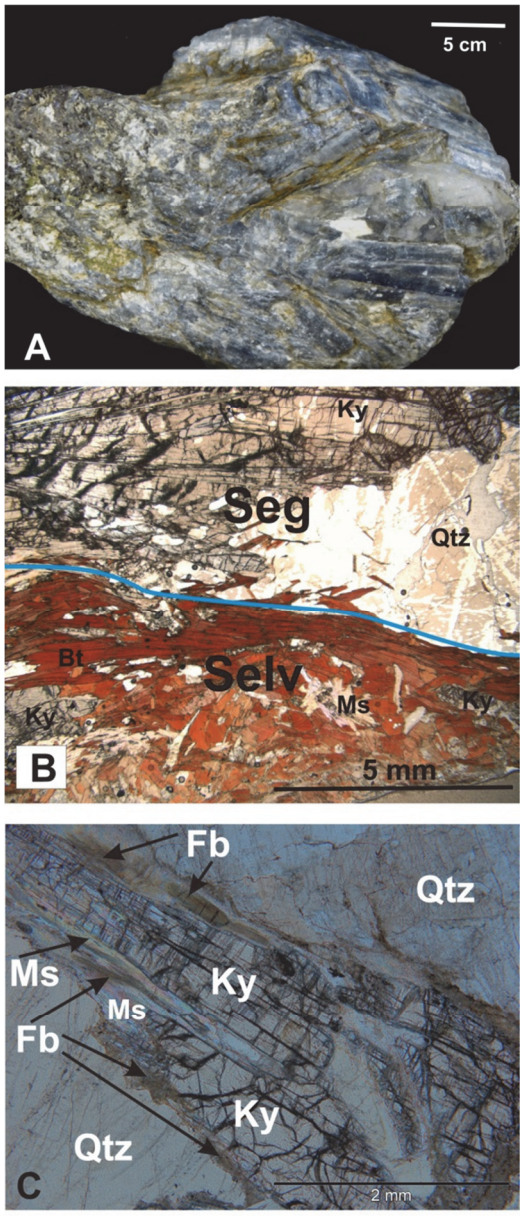

Fig. 3. Microphotographs of kyanite-quartz segregations. A. Kyanite crystals < 12 cm long. B. Kyanite-quartz segregation (Seg) bordered by biotite-rich selvage (Selv). C. Kyanite crystals (Ky) overgrown by muscovite (Ms) and fibrolite (Fb), all wrapped by quartz (Qtz).

TABLE 1

Chemical composition (wt%) and crystal-chemical formulae of kyanite.

Sample	LoD	Ky_1	Ky_2	Ky_3	Ky_4	Ky_5	Ky_6	Ky_7	Ky_8	Ky_9
SiO_2	0.03	37.24	37.15	37.28	37.01	37.02	37.27	37.35	37.53	37.27
Al_2O_3	0.03	63.34	62.74	62.66	62.58	63.09	63.00	62.88	62.95	62.56
FeO	0.15	-	-	-	0.20	0.21	-	-	-	0.27
Total		100.58	99.89	99.94	99.79	100.32	100.27	100.23	100.48	100.11
crystal-chemical formulae recalculated to 20 O^{2-}										
Si		3.990	4.01	4.017	4.004	3.985	4.007	4.019	4.021	4.020
Al^{IV}		4.010	3.990	3.983	3.996	4.015	3.993	3.981	3.979	3.980
Al^{VI}		3.988	3.991	3.973	3.983	3.989	3.991	3.994	3.971	3.973
Fe^{2+}		-	-	-	0.018	0.019	-	-	-	0.024

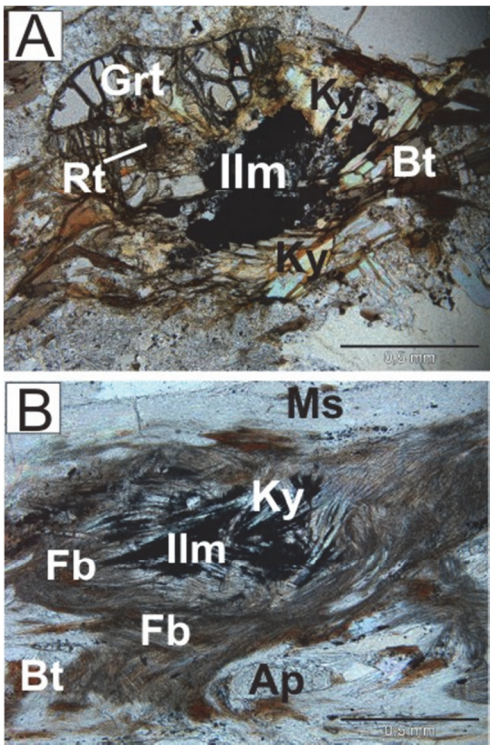

Fig. 4. Microphotographs showing phase relations. A. Kyanite (Ky) and ilmenite (Ilm) growing at the expense of almandine-garnet (Grt) and rutile (Rt). Biotite (Bt) also present. B. Ilmenite (Ilm) and kyanite (Ky) bordered by fibrolite (Fb) and muscovite (Ms). Biotite (Bt) and accessory apatite (Ap) also present.

TABLE 2

Chemical composition (wt%) and crystal-chemical formulae of muscovite Ms_1 in the kyanite-quartz segregations and muscovite Ms_2 in the selvage.

Sample	Muscovite 1						Muscovite 2			
	LoD	Ms1_1	Ms1_2	Ms1_3	Ms1_4	Ms1_5	Ms2_1	Ms2_2	Ms2_3	Ms2_4
SiO_2	0.03	46.06	46.80	47.72	45.85	46.12	46.73	46.77	47.58	46.77
TiO_2	0.05	0.35	0.37	0.40	0.33	1.02	-	-	-	-
Al_2O_3	0.03	30.31	31.25	31.10	36.81	36.03	36.84	36.60	35.58	37.17
MgO	0.02	2.94	2.41	2.72	0.59	-	0.40	0.39	0.74	0.37
FeO	0.16	3.86	2.80	2.01	1.11	0.57	0.63	0.46	0.61	0.54
Na_2O	0.03	0.08	0.16	0.27	1.19	1.04	1.46	1.27	0.77	1.53
K_2O	0.06	10.54	10.67	10.46	9.52	9.87	9.55	9.38	9.78	9.33
H_2O_{calc}		4.38	4.43	4.46	4.54	4.55	4.56	4.54	4.55	4.58
Total		98.52	98.87	99.14	99.93	100.08	100.17	99.40	99.62	100.29
crystal-chemical formulae recalculated to 22 O^{2-}										
Si		6.305	6.339	6.412	6.06	6.086	6.148	6.178	6.272	6.128
Ti		0.036	0.037	0.04	0.033	0.102	-	-	-	-
Al^{IV}		1.695	1.661	1.588	1.94	1.914	1.852	1.822	1.728	1.872
Al^{VI}		3.195	3.327	3.336	3.794	3.689	3.859	3.876	3.800	3.869
Mg		0.600	0.486	0.545	0.116	-	0.078	0.077	0.146	0.073
Fe		0.442	0.317	0.226	0.122	0.112	0.069	0.051	0.068	0.059
Na		0.022	0.041	0.07	0.306	0.265	0.372	0.326	0.196	0.389
K		1.841	1.844	1.792	1.604	1.661	1.603	1.581	1.645	1.560

4.1.2. Selvages

Selvages bordering the kyanite-quartz segregations (Fig. 3b) are composed of biotite (Bt_2: *#fm* = 0.506-0.551; Ti = 0.192-0.272 a.p.f.u.; Table 4), plagioclase and fibrolitic sillimatite, and porphyroblasts of almandine garnet (Grt_2: $Alm_{74}Spes_5Py_7Gros_{14}$ - $Alm_{74}Spes_7Py_{15}Gros_3$; Table 3). Locally, kyanite crystals, < 0.5 mm in length, are associated with ilmenite that is partially replaced by sillimanite and muscovite (Fig. 4a, b).

Accessories are represented by K-feldspar ($Or_{76}Ab_{24}$ - $Or_{97}Ab_3$), ilmenite with Mn substitution in the range of 0.30-0.33 a.p.f.u (Table 5), (Ca,F)-apatite with < 0.23wt% Y_2O_3 and < 0.24wt% MnO, and rutile.

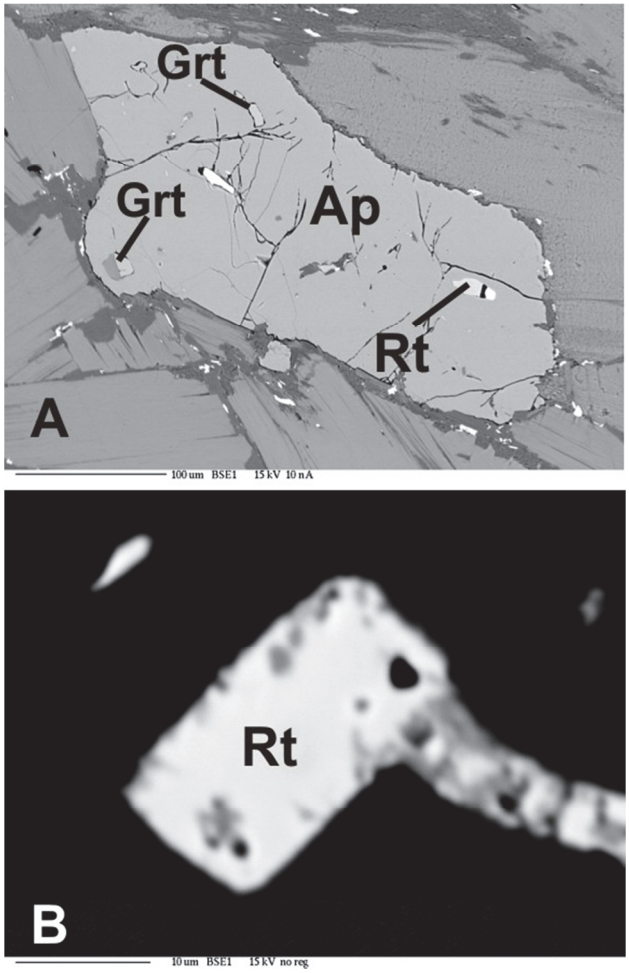

Fig. 5. A. Apatite (Ap) with garnet (Grt) and rutile (Rt) inclusions. B. Rutile crystal. (BSE images).

Secondary muscovite (Ms_2) replacing the Al_2SiO_5 polymorphs (Fig. 3c, 4b) shows a simple chemical composition (Table 2). Secondary chlorite replacing biotite along cleavage planes is (Mg, Fe)-chlorite from the groups of ripidolite, picnochlorite and diabantine (*#fm* = 0.485-0.785).

TABLE 3

Chemical composition (wt%) and crystal-chemical formulae of garnet Grt_1 from apatite inclusions and Grt_2 present as porphyroblasts in the selvage.
* Analyses used for geothermometry. Values of Fe^{3+} and Fe^{2+} are result of microprobe analyses.

Sample	Grt1			Grt2						
	LoD	*Grt1_1	*Grt1_2	Grt2_1	Grt2_2	Grt2_3	Grt2_4	Grt2_5	Grt2_6	Grt2_7
SiO_2	0.01	35.71	36.53	37.48	37.57	37.18	37.71	37.50	37.40	37.66
Al_2O_3	0.01	19.46	19.59	21.24	21.19	21.32	21.28	21.30	21.62	21.81
Fe_2O_3	0.07	1.64	1.60	-	0.08	-	-	0.04	-	-
FeO	0.07	28.59	30.83	33.21	32.86	33.33	32.37	33.19	33.56	33.71
CaO	0.02	3.53	1.70	4.91	5.12	5.02	5.04	4.98	1.16	1.12
MnO	0.07	8.28	7.11	2.05	2.04	1.89	1.98	2.00	3.73	2.91
MgO	0.01	1.50	1.97	1.91	2.06	2.17	2.02	2.13	3.15	3.91
Total		98.71	99.33	100.79	101.00	100.94	100.49	101.17	100.61	101.11
Formulae recalculated to 24 O^{2-}										
Si		5.920	6.000	5.989	5.987	5.942	6.021	5.971	5.963	5.975
Al		3.800	3.790	4.001	3.98	4.014	4.004	3.997	4.069	4.071
Fe^{3+}		0.200	0.200	-	0.009	-	-	0.005	-	-
Fe^{2+}		3.970	4.230	4.438	4.379	4.455	4.322	4.42	4.464	4.484
Ca		0.630	0.300	0.841	0.874	0.86	0.861	0.85	0.189	0.199
Mn		1.160	1.000	0.277	0.275	0.256	0.267	0.27	0.39	0.504
Mg		0.370	0.480	0.456	0.49	0.517	0.48	0.505	0.924	0.751
X_{py}		0.058	0.077	0.074	0.082	0.086	0.080	0.084	0.154	0.125
X_{alm}		0.627	0.681	0.738	0.728	0.741	0.719	0.735	0.743	0.746
X_{spes}		0.183	0.161	0.046	0.046	0.042	0.044	0.045	0.065	0.084
X_{gross}		0.099	0.048	0.140	0.145	0.143	0.143	0.141	0.031	0.033
X_{adr}		0.032	0.032	0	0.001	0	0	0.001	0	0
$T[ºC]_{FS}$		432.1	492.5	-	-	-	-	-	-	-
$T[ºC]_{IM}$		506.6	529.8	-	-	-	-	-	-	-

LoD - limits of detection. X_{py} = Mg/(Ca + Mn + Mg + Fe); X_{alm} = Fe^{2+}/(Ca + Mn + Mg + Fe); X_{spes} = Mn/(Ca + Mn + Mg + Fe); X_{gross} = Ca/(Ca + Mn + Mg + Fe); X_{adr} = Fe^{3+}/(Ca + Mn + Mg + Fe); $T[ºC]_{FS}$- temperatures estimate by using Ferry and Spear geothrmometer; $T[ºC]_{IM}$- temperatures estimate by using Indares and Martignole (1985) geothermometer

TABLE 4

Chemical composition (wt%) and crystal-chemical formulae of biotite inclusions in the segregation (Bt_1) and from the selvage (Bt_2) with temperatures computed according to the Ti-in-Bt geotermometer of Henry et al. (2005). * Analyses used for geothermometry.

		Biotite 1		Biotite 2						
Sample	LoD	*Bt1_1	*Bt1_2	Bt2_1	Bt2_2	Bt2_3	Bt2_4	Bt2_5	Bt2_6	Bt2_7
SiO_2	0.03	34.68	35.09	35.24	36.05	35.20	35.53	35.62	36.27	36.39
TiO_2	0.06	2.01	1.88	2.38	2.01	2.06	2.11	1.98	1.70	1.78
Al_2O_3	0.02	19.91	20.20	19.24	18.90	18.89	19.15	19.11	21.70	21.72
FeO	0.16	19.53	19.30	20.16	18.76	19.68	19.46	19.94	16.65	16.35
MnO	0.17	0.22	0.19	-	-	0.19	0.22	-	-	-
MgO	0.03	9.30	8.84	9.23	9.67	9.66	9.73	9.73	8.70	8.94
Na_2O	0.05	0.12	0.14	0.19	0.18	0.18	0.21	0.17	0.23	0.16
K_2O	0.03	8.96	8.89	9.06	8.95	8.90	8.97	9.08	9.19	9.35
H_2O		3.92	3.93	3.95	3.95	3.92	3.96	3.96	4.00	4.01
Total		98.71	98.61	99.44	98.46	98.70	99.32	99.60	98.44	98.70
crystal-chemical formulae recalculated to 22 O^{2-}										
Si		5.304	5.356	5.353	5.476	5.379	5.382	5.39	5.441	5.441
Ti		0.232	0.215	0.272	0.229	0.237	0.24	0.225	0.192	0.201
Al^{IV}		2.696	2.644	2.647	2.524	2.621	2.618	2.61	2.559	2.559
Al^{VI}		0.893	0.991	0.798	0.861	0.782	0.8	0.798	1.278	1.268
Fe^{2+}		2.498	2.464	2.562	2.383	2.515	2.465	2.524	2.089	2.045
Mn		0.029	0.024	-	-	0.025	0.028	-	-	-
Mg		2.120	2.011	2.09	2.191	2.201	2.198	2.194	1.946	1.993
Na		0.037	0.042	0.055	0.052	0.053	0.06	0.051	0.068	0.045
K		1.748	1.731	1.756	1.735	1.735	1.734	1.753	1.758	1.784
fm		0.544	0.553	0.551	0.523	0.536	0.531	0.536	0.518	0.506
X_{Mg}		0.367	0.352	0.365	0.385	0.382	0.383	0.381	0.353	0.362
X_{Fe}		0.433	0.432	0.448	0.419	0.437	0.430	0.439	0.379	0.371
X_{Ti}		0.040	0.038	0.047	0.040	0.041	0.042	0.039	0.035	0.036
T[ºC]				638.8	613.5	617.3	620.6	607.0	578.8	591.3

fm = $(Fe^{2+} + Mn)/(Fe^{2+} + Mn + Mg)$; $X_{Mg} = Mg/(Ti + Mn + Mg + Fe^{2+} + Al^{VI})$; $X_{Fe} = Fe^{2+}/(Ti + Mn + Mg + Fe^{2+} + Al^{VI})$; $X_{Ti} = Ti/(Ti + Mn + Mg + Fe^{2+} + Al^{VI})$; LoD - limits of detection.

TABLE 5

Chemical composition (wt%) and crystal-chemical formulae of ilmenite.

Sample	LoD	Ilm_1	Ilm_2	Ilm_3	Ilm_4	Ilm_5	Ilm_6
TiO_2	0.03	53.89	54.30	54.07	53.49	56.36	54.30
FeO	0.07	38.09	37.44	38.71	38.35	33.64	34.01
MnO	0.07	7.59	7.14	7.02	7.74	7.18	8.74
Total		99.57	98.88	99.80	99.58	97.46	97.89
crystal-chemical formulae recalculated to 6 O^{2-}							
Ti		2.03	2.06	2.04	2.02	2.128	2.057
Fe		1.6	1.58	1.62	1.61	1.412	1.433
Mn		0.32	0.3	0.3	0.33	0.305	0.373

LoD - limits of detection.

4.1.3. Phase relations and geothermometry

The assemblage rutile + almandine garnet occurs as inclusions in apatite (Fig. 5a) and kyanite. In the host metapelites, kyanite and ilmenite growing at the expence of garnet and rutile are observed (Fig. 4a) while, in the selvage, complete pseudomorphs after garnet + rutile are evident (Fig. 4b). In the kyanite-quartz segregations, rutile and garnet are

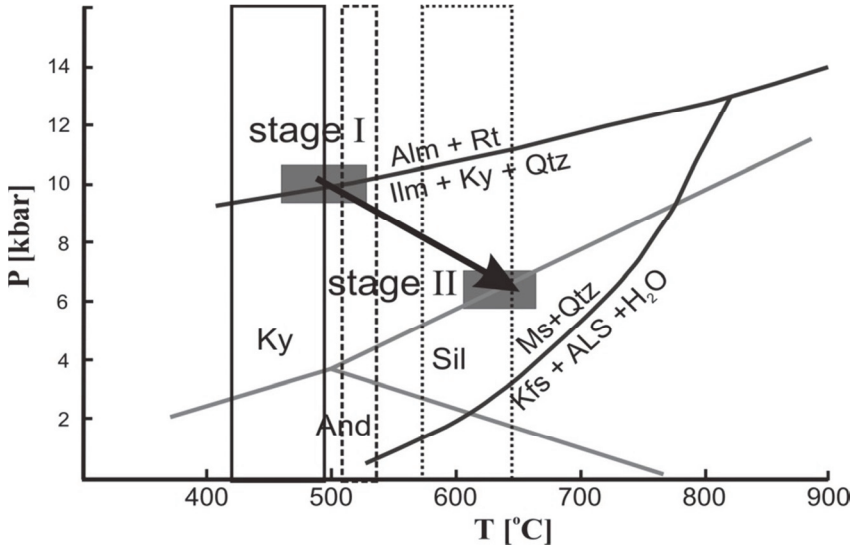

Fig. 6. P-T path of the kyanite-quartz segregation formation: solid line – Grt-Bt geothermometry by Ferry and Spear (1978), dashed line – Grt-Bt geothermometry by Indares and Martignole (1985), dotted line - Ti-in-Bt geothermometry by Henry et al. (2005). Stage I (higher pressure (above 9 kbar) – formation of the kyanite-quartz segregations; Stage II (pressure dropped to 5-4 kbars and shifted to higher temperatures) – connected with uplift and granitoid intrusion.

preserved only as inclusions in apatite and in kyanite. Garnet Grt_1 and biotite Bt_1 inclusions are in chemical balance and were used to estimate the temperature (Table 3 and 4). The method of Ferry and Spear (1978) gives temperatures in the range 432-492ºC whereas the calibration by Indares and Martignole (1985) yields temperatures in the range 507-530ºC (Fig. 6). The first method was used to provide better comparison with the classical localities in the Alps (Allaz et al. 2005). The second incorporates adjustment for the higher Mn contents in garnet and for Ti and Al^{VI} in biotite.

The kyanite-quartz segregations are bordered by biotite selvages. The fact that the biotite (Bt_2) in them is enriched in Ti enables use of the geothermometric calibration based on the Ti content in biotite proposed by Henry et al. (2005). The temperatures yielded lie in the range 579-639ºC (Table 4, Fig. 6). The chlorite growing locally at the expence of biotite is evidence of retrogression. The Cathelineau and Nieva (1985) and Ruggieri (2010) calibrations provide temperature estimates of 300-400ºC and 280-320ºC, respectively, for the chloritisation.

Muscovite overgrowths and submicroscopic muscovite crystals occur along cleavage plains and cracks in kyanite. Fibrolitic sillimanite (Fig. 3c, 4b) and K-feldspar are seen to have replaced that muscovite according to the reaction Ms + Qtz → Sil + Kfs + H_2O.

4.2. Trace elements and kyanite luminescence

Trace elements influence kyanite color and cause luminescence. Usually, the luminescence color depends on the presence of Ti, Fe, and Cr (Müller et al. 2011). Ti, Fe, Cr and Mn ions usually substitute for Al in structurally different positions. V may replace Al if it is in a higher oxidation state (V^{5+}; Gaft et al. 2012; Neiva 1984).

Twenty four analysis revealed the presence of the following trace elements in the kyanite: ^{23}Na, ^{24}Mg, ^{39}K, ^{44}Ca, ^{47}Ti, ^{51}V, ^{52}Cr, ^{55}Mn, ^{56}Fe (Table 6). The mineral contains significant amounts of Fe, Cr, Ti and V. Mn and Ti are positively correlated ($r^2 = 0.857$). A strong positive correlation of Fe and Ti is seen where Ti content is low (< 90 ppm; $r^2 = 0.821$). Iron is also positively correlated with Cr ($r^2 = 0.724$) and V ($r^2 = 0.864$). V substitution in the Al position is possible only for V^{5+}; its ionic radius (59 Å) most closely compares with that of Al^{3+} (Pearson, Shaw 1960). Both Cr and V substitutions cause the pinkish-violet-blue luminescence of the analysed kyanite (Fig. 7).

4.3. Whole-rock chemical composition

For this study, the kyanite-quartz segregation (Seg), selvage (Selv) and mylonitised host-rock (garnet-bearing gneiss) were analysed for major and trace elements. Silica content in the kyanite-quartz segregation and in the surrounding gneiss is high whereas that of aluminium is moderate (Table 7). In the selvage, the aluminium content is the highest,

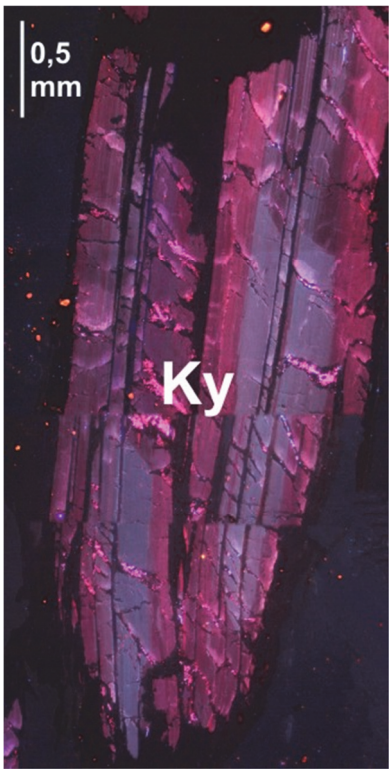

Fig. 7. Cathodoluminescence image of kyanite crystal.

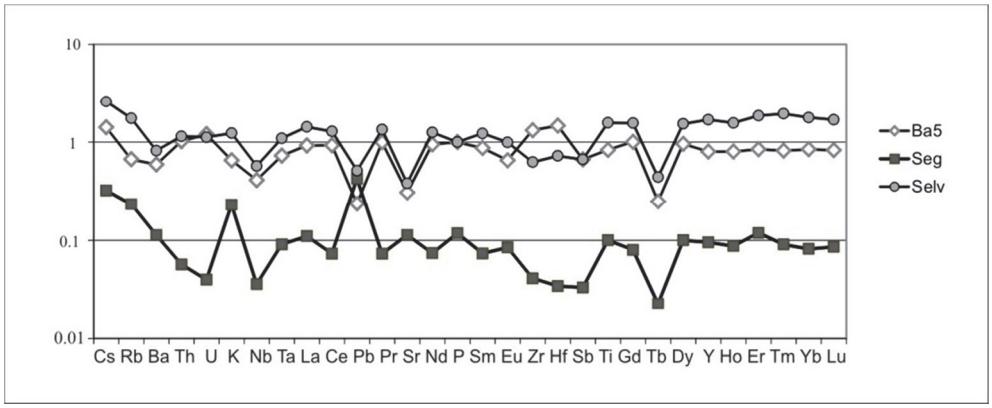

Fig. 8. Trace-element spider diagrams for gneiss (Ba5), kyanite-quartz segregation (Seg) and selvage (Selv). Normalized to continental upper crust (Taylor, Mc Lennan 1981)

due to the abundant presence of Al-rich biotite, almandine garnet, fibrolite, kyanite remnants and secondary muscovite (Fig. 4). The high iron content in the selvage reflects the concentrations of biotite (*#fm* = 0.506-0.551; Table 4) and almandine garnet (Table 3).

HFSE elements are more concentrated in the selvage than in the gneiss (Fig. 8) whereas, excepting Cr, they are impoverished in the kyanite-quartz segregations (Table 7; Fig. 8). Chondrite (C1)-normalized rare-earth element (REE) patterns for the selvage, in their similar ranges of REE fractionations and their Eu anomalies (Fig. 9), mirror those of the gneiss. The kyanite segregation has the lowest REE content and a REE fractionation pattern similar to that of the gneiss, except for a nearly absent Eu anomaly (Eu/Eu* = 0.95; Fig. 9).

TABLE 6

Trace elements in kyanite (in ppm).

	Na	Mg	K	Ca	Ti	V	Cr	Mn	Fe
LoD	14.3	0.9	8.3	1.7	1.2	0.01	0.01	0.1	1.1
Ky1	58.2	114.2	74.9	158.2	95.8	100.9	107.0	5.1	1290.6
Ky2	-	87.1	59.2	112.7	90.1	106.1	98.8	2.2	1334.2
Ky3	-	79.6	71.4	112.6	100.5	99.1	117.9	5.1	1432.5
Ky4	-	103.8	85.1	96.1	104.1	100.2	110.3	7.5	1510.6
Ky5	-	81.4	-	24.7	16.3	83.9	80.3	0.0	998.0
Ky6	73.9	84.5	149.1	300.6	17.4	100.0	87.9	1.3	1061.0
Ky7	91.1	117.8	206.4	138.7	56.8	119.8	98.4	2.3	1653.2
Ky8	93.6	104.3	216.0	132.1	26.2	99.6	114.6	1.5	1170.0
Ky9	50.3	104.7	460.1	232.8	37.5	129.1	87.4	4.1	1490.9
Ky10	61.2	90.0	169.6	84.4	41.4	110.4	125.7	1.5	1363.5
Ky11	30.1	80.9	174.9	108.4	26.1	106.8	97.0	3.8	1184.9
Ky12	43.2	77.8	20.3	-	23.3	94.3	139.9	0.0	1095.0
Ky13	35.4	89.1	22.5	-	46.9	125.7	123.3	1.5	1228.1
Ky14	-	93.3	35.9	-	32.3	96.6	95.9	1.4	1082.4
Ky15	139.6	83.1	233.9	124.6	32.0	102.2	128.3	2.4	1119.0
Ky16	34.0	63.2	88.8	113.3	28.4	95.9	114.2	1.0	984.3
Ky17	-	138.3	20.1	4.5	48.0	146.4	121.0	1.8	1591.3
Ky18	-	124.9	26.4	47.4	56.9	157.6	151.9	1.1	1590.1
Ky19	-	129.1	41.6	17.2	58.9	134.0	121.0	0.8	1427.6
Ky20	136.2	141.4	310.4	361.6	64.6	135.2	145.2	4.4	1692.9
Ky21	-	131.5	-	66.1	86.8	135.3	109.6	1.9	1477.3
Ky22	-	104.5	-	45.8	105.7	113.5	95.1	1.5	1219.2
Ky23	75.7	115.9	132.4	185.5	66.9	160.2	158.2	2.8	1645.1
Ky24	22.2	190.5	149.1	73.7	64.4	154.3	163.4	3.2	1691.9

LoD - limits of detection.

TABLE 7

Major- and trace-elements composition of kyanite-quartz segregation (Seg), selvage (Selv) and garnet-bearing gneiss (Ba5). Oxides in wt%, trace elements in ppm.

Sample	LoD	Ba5	Seg	Selv
SiO_2	0.01	77.6	87.2	54.9
TiO_2	0.01	0.50	0.06	0.94
Al_2O_3	0.01	11.19	9.69	23.22
Fe_2O_3	0.04	2.96	0.82	8.45
MnO	0.01	0.03	0.01	0.08
MgO	0.01	1.12	0.22	3.58
CaO	0.01	0.51	0.11	0.64
Na_2O	0.01	1.83	0.26	0.98
K_2O	0.01	2.16	0.76	4.06
P_2O_5	0.01	0.17	0.02	0.17
LOI	0.01	2.00	0.80	2.70
Total		100.03	99.99	99.72
Sr	0.5	102.90	37.70	127.00
Ba	0.1	415.00	79.00	573.00
Rb	0.1	73.70	25.70	191.50
Th	0.2	10.70	0.60	12.00
U	0.1	3.00	0.10	2.80
Zn	0.1	33.00	15.00	89.00
Pb	0.1	3.50	6.30	7.60
Ga	0.5	12.60	5.80	27.00
Cr	20	95.80	130.00	116.30
V	8.0	49.00	28.00	138.00
Zr	0.1	316.00	9.90	150.20
Hf	0.1	8.50	0.20	4.20
Y	0.1	17.60	2.10	37.10
La	0.1	27.70	3.30	42.70
Ce	0.1	55.70	4.40	76.90
Pr	0.02	6.67	0.49	8.98
Nd	0.3	25.60	2.00	33.80
Sm	0.05	4.61	0.39	6.48
Eu	0.02	0.85	0.11	1.29
Gd	0.05	4.02	0.32	6.22
Tb	0.01	0.55	0.05	0.97
Dy	0.05	3.64	0.38	5.81
Ho	0.02	0.64	0.07	1.25
Er	0.03	1.78	0.25	3.89
Tm	0.01	0.27	0.03	0.64
Yb	0.05	1.86	0.18	3.90
Lu	0.01	0.29	0.03	0.59

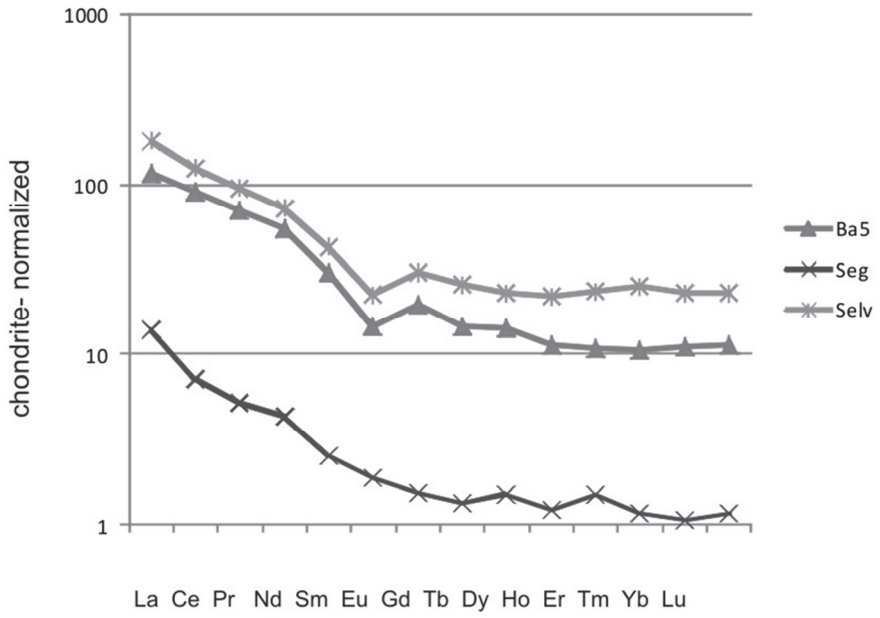

Fig. 9. Chondrite-normalized REE patterns for gneiss (Ba5), kyanite-quartz segregation (Seg) and selvage (Selv) (Sun, McDonough 1989).

5. Discussion

5.1. Phase relations and decompression conditions

The rutile + almandine assemblage occurring as inclusions and replaced by kyanite + ilmenite + quartz has been deemed to be the result of a pressure drop from > 9 kbar. The lack of andalusite indicates a pressure above 4 kbar (Pyka et al. 2013a, b; Spear 1993; Yardley 1989). This is in agreement with the earlier P-T reconstructions for the rocks of the area. Janák et al. (1996, 2001) estimated metamprphic conditions in the Upper Unit at 670-700ºC and 10-15 kbar with marked decompression at 4-5 kbar. Moussalam et al. (2012) documented a decompression path from 16 to 8 kbars and a post-intrusive cooling rate of ~ 30ºC/Ma. These results are also consistent with the decompression history from 9-7.5 kbar documented for the northern part of the metamorphic complex (Burda, Gawęda 1999; Burda, Gawęda 2009).

The temperature range computed based on the garnet-biotite geothermometry (432-492ºC and 507-530ºC; Fig. 6) is similar to that obtained by Allaz et al. (2005) for similar kyanite-quartz veins in the Central Alps and by Whitney (2002) for kyanite-andalusite-sillimanite-quartz segregations in the metapelitic Sivrihisar Formation in Turkey. Temperatures of 579-639ºC computed from Ti content in low-to-medium pressure metapelitic biotites (Fig. 6) by Henry et al. (2005) are close to those obtained by Janák et al. (1996, 2001) from the Tatras. However, it is worth noting that the composition of biotite in

metapelites may be quite easily reset by heat from, e.g. a granite intrusion (Lavaure, Sawyer 2011) as is the case in the Tatra Mountains metamorphic rocks (Gawęda 2009). Thus, the Ti-biotite temperatures reported here might be alternatively interpreted as reflecting cooling after decompression and re-heating (Gawęda 2009).

The temperatures of biotite chloritization, estimated using the Cathelineau and Nieva (1985) and Ruggieri (2010) calibrations as 300-400ºC and 280-320ºC, respectively, are similar (within cumulative errors) to those obtained from the granitoid (Gawęda, Włodyka 2012), and represent the retrogression path for the metapelitic rocks of Baranèc Mt.

5.2. Formation of kyanite-quartz segregations

Two-step major-element mass-balance calculations were performed. In the first step, the percentages of minerals participating in the segregations were established by modal analysis (Table 8a). Predominant quartz (79%) is accompanied by kyanite (8%), muscovite (12%) and plagioclase (1%). That composition was used for the next step of modelling to assess the mobility of major elements, following the method used for mass balance calculations (e.g. Olsen 1984; Burda,Gawęda 1997). As the measured proportion of biotite-rich selvage in relation to the whole segregation volume was about 11%, the volume proportion (11:89) was used as a default. The resulting mass-balance calculations (Table 8b) reveal that the Al content was almost stable in the selvage + segregation system whereas the other elements were mobilized. SiO_2 mobility was especially remarkable (83%) as is reflected in the predominance of quartz in the segregation (Tables 7, 8b). Thus, SiO_2, together with other mobile elements such as Fe, Na and K are responsible for the

TABLE 8a

Modal composition of the kyanite-quartz segregation compared to computed composition based on major-element chemistry for segregation (S_N), surrounding rocks (Ba5) and selvage (Selv); S_C - chemistry of the calculated segregations; balance (B) = S_C - S_N.

	Ky	Qtz	Bt	Ms	Pl	Ba5	S_N	Selv	S_C	B	B^2
SiO_2	37.21	100	35.62	46.7	63.54	79.1	87.95	56.6	88.22	-0.3	0.071
TiO_2			1.98	0.1	0	0.51	0.06	0.97	0.012	0.05	0.002
Al_2O_3	62.63		19.11	36.84	22.9	11.41	9.77	23.93	9.660	0.1	0.012
Fe_2O_3	0.16		19.94	0.62	0	3.02	0.83	8.71	0.087	0.7	0.552
MnO			0.11		0	0.03	0.01	0.08	0	0.0	0.000
MgO			9.73	0.4	0	1.14	0.22	3.69	0.048	0.2	0.029
CaO			0		4.22	0.52	0.11	0.66	0.042	0.1	0.005
Na_2O			0.17	1.46	9.25	1.87	0.26	1.01	0.268	0.0	0.000
K_2O			9.08	9.55	0.11	2.20	0.77	4.18	1.147	-0.4	0.142
P_2O_5			0		0	0.17	0.02	0.18	0	0.0	0.000
Total	100.0	100.0	99.7	100.1	100.0	99.99	100.0	100.0	99.48		0.814
MSWD											0.902

TABLE 8b

Mass balance calculation assuming volume proportion of selvage (Selv) to the segregation (S_N) is 11:89; all values are in wt%.

	%Selv	%S	Sum	Ba5	Balance	B^2
SiO_2	6.2249	78.2755	84.5004	79.1	5.4	28.949
TiO_2	0.1067	0.0534	0.1601	0.51	-0.3	0.122
Al_2O_3	2.6323	8.6953	11.3276	11.41	-0.082	0.007
Fe_2O_3	0.9581	0.7387	1.6968	3.02	-1.3	1.751
MnO	0.0088	0.0089	0.0177	0.03	0.0	0.000
MgO	0.4059	0.1958	0.6017	1.14	-0.5	0.290
CaO	0.0726	0.0979	0.1705	0.52	-0.3	0.122
Na_2O	0.1111	0.2314	0.3425	1.87	-1.5	2.333
K_2O	0.4598	0.6853	1.1451	2.20	-1.1	1.113
P_2O_5	0.0198	0.0178	0.0376	0.17	-0.1	0.017
						34.704
MSWD			5.891			

MSWD = $\sqrt{\sum B^2}$ (according to York 1969; Burda, Gawęda 1997)

relatively high √MSWD value (5.89; Table 8b), implying that the analysed chemical system was open. However, all elements showing high degrees of change (Si, Fe, Na, K) are generally considered as quite easy to mobilize during metamorphism. Cr^{3+} shows similar behaviour to Fe^{3+} and V^{5+} suggesting that all three migrated together, resulting in the kyanite luminescence (Fig. 7). That could be interpreted as a result of high oxygen fugacity at the segregation-forming stage enabling the incorporation of Cr^{3+} and V^{5+} into the kyanite structure. The aluminium remains stable, suggesting that the diffusion, and the associated mass transfer, was limited. As it was mentioned in paragraph 4.3, the kyanite-quartz segregations have the lowest (ten times lower) REE content (Fig. 8, 9). It is caused by the fact that kyanite and quartz do not accumulate REE.

The observations mentioned above and in paragraph 5.1 favour a HP origin for veins, as proposed elsewhere by Widmer and Thompson (2001). The dissolution, transport and re-precipitation of mineral phases (in small fissures growing in response to local pressure gradients) caused local mass transfer due to the migration of fluid released by mineral dehydration. We conclude that the kyanite-quartz segregations were formed in a similar way, with mobilization of fluids during decompression of the Tatra Massif, playing the most important role in the process (stage I in Fig. 6).

After the kyanite-quartz segregations formed, the growth of sillimatite and biotite recrystallization was promoted by heat from the granitoid intrusion (stage II in Fig. 6). Fluids circulating during post-orgenic cooling caused the secondary alterations, i.e. the growth of secondary muscovite and chlorite.

6. Conclusions

1. Kyanite-quartz segregations in metapelites in the Tatra Mountains were formed as a result of the activity of fluids of local origin, characterized by high oxygen fugacity and generated during dehydration of the metapelitic rocks during uplift. The main mechanism was likely diffusion-driven mass-transfer to extension-related cracks and fissures.
2. Heating and further decompression during Variscan granitoid intrusion led to the formation of sillimanite at 579-639ºC as the pressure dropped to 5-4 kbars. The further cooling path was concordant with the general trend for the entire Tatra Massif.

7. Acknowledgements

Piotr Dzierżanowski PhD and Mrs Lidia Jeżak are thanked for their help during the microprobe work. The authors benefitted from discussions on trace-element interpretation with prof. Maria Czaja. This study was financially supported by National Science Centre (NCN) grant 2012/07/B/ST10/ 04366 (to Aleksandra Gawęda). Acknowledgements to Padhraig Kennan for English corrections and to Reviwers who contributed to improvement of the paper.

8. References

Allaz, J., Maeder, X., Vannay, J.C., & Steck, A. (2005). Formation of aluminosilicate-bearing quartz veins in the Simano nappe (Central Alps): structural, thermobarometric and oxygen isotope constraints. *Schweizerische Mineralogische und Petrographische Mitteilungen*, *85*, 191-214.

Ague, J. J. (2011). Extreme channelization of fluid and the problem of element mobility during Barrovian metamorphism. *American Mineralogist, 96*, 333-352. DOI: 10.2138/am.2011.3582.

Burda, J., & Gawęda, A. (1997). Mass-balance calculations in migmatites from the Upper Kościeliska Valley (The Western Tatra Mts., S-Poland). *Mineralogia Polonica, 28*(1)*,* 53-68.

Burda, J., & Gawęda, A. (1999). Petrogeneza migmatytów z Górnej części Doliny Kościeliskiej w Tatrach Zachodnich. *Archiwum Mineralogiczne, 52*(2), 163-194.

Burda, J., & Gawęda, A. (2009). Shear-influenced partial melting in the Western Tatra metamorphic complex: Geochemistry and geochronology. *Lithos, 110*, 373-385. DOI: 10.1016/j.lithos.2009.01.010.

Burda, J., Gawęda, A., & Klötzil, U. (2011). Magma hybridization in the Western Tatra Mts. granitoid intrusion (S-Poland, Western Carpathians). *Mineralogy and Petrology, 103*, 19-36. DOI 10.1007/s00710-011-0150-1.

Burda, J., Gawęda, A., & Klötzil, U. (2013). U-Pb zircon age of the youngest magmatic activity in the High Tatra granites (Central Western Carpathians). *Geochronometria, 40*(2), 134-144. DOI 10.2478/s13386-013-0106-9.

Cathelineau, M., & Nieva, D. (1985). A chlorite solid solution geothermometer the Los Azufres (Mexico) geothermal system. *Mineralogy and Petrology, 91*, 235-244.

Deditius, A. (2004). Petrology and isotopic age of the muscovite blasthesis from the mylonitic zones in the crystalline rocks of the Western Tatra Mountains). *Geologia* 16. University of Silesia publishing House (in Polish, English abstract).

Ferry, J. M., & Spear, F. S. (1978). Experimental calibration of the partitioning of Fe and Mg between biotite and garnet. *Mineralogy and Petrology, 66*, 113-117.

Gaft, M., Strek, W., Nagli, L., Panczer, G., Rossma, G.R., & Marciniak, L. (2012). Laser-induced time-resolve luminescence of natural sillimanite Al_2SiO_5 and synthetic Al_2SiO_5 activated by chromium. *Journal of luminescence, 132*, 2855-2862. DOI 10.1016/j.jlumin.2012.04.045.

Gawęda, A. (2009). *Enklawy w granicie Tatr Wysokich* (ed.3). Katowice: Wydawnictwo Uniwersytetu Śląskiego.

Gawęda, A., & Burda, J. (2004). Ewolucja metamorfizmu i deformacji w kompleksie krystalicznym Tatr Zachodnich. *Geologia*, *16*, 153-185.

Gawęda, A., & Włodyka, R. (2012). The origin of post magmatic Ca-Al minerals in granite- diorite mingling zones: the Tatra granitoid intrusions, Western Carpathians. *Neues Jahrbuch für Mineralogie-Abhandlungen, 190*(1), 29-47. DOI 10.1127/0077-7757/2012/0228.

Gawęda, A., & Kozłowski, K. (1998). Magmatic and metamorphic evolution of the Polish part of the Western Tatra crystalline basement (S-Poland, W-Carpathians). *XVI Congress of CBGA, Wienna*, 117.

Gawęda, A., & Golonka, J. (2011). Variscan plate dynamics in the circum- Carpathian area. *Geodynamica Acta, 24*, 141-155. DOI: 10.3166/ga.24.141-155.

Gawęda, A., & Szopa, K. (2011). The origin of magmatic layering in the High Tatra granite, Central Western Carpathians – implications for the formation of granitoid plutons. *Transactions of the Royal Society of Edinburgh Earth Sciences,102*, 1-16. DOI 10.1017/S1755691012010146.

Gorek, A. (1956). Geologicka Stavba Zapadnych Tatier. Geologický Sbornik Slovenske Akadémie Vied. Bratislava, VII.

Gorek, A. (1969). Postavenie zvyskov metamorfovaneho plasta v granitoidnom masive Vysokych Tatier a ich vztah v Zapadnych Tatrach. *Geologica, 4,* 103-115.

Henry, D. J., Guidotti, Ch., & Thomson, J. A. (2005). The Ti-saturation surface for low-to-medium pressure metapelitic biotites: Implications for geothermometry and Ti-substitution mechanisms. *American Mineralogist, 90*, 316-328. DOI: 10.2138/am.2005.1498.

Indares, A., & Martignole, J. (1985). Biotite- garnet geotermometry in the granulite facies: the influence of Ti and Al in biotite. *American Mineralogist, 70*, 272-278.

Janák, M., O`Brien, J. P., Hurai, V., & Reutel, C. (1996). Metamorphic evolution and fluid composition of garnet-clinopyroxene amphibolites from the Tatras Mountains, Western Carpathians. *Lithos, 39*, 57-79.

Janák, M., Plasienka, D., & Petrik, I. (2001). Extrusion to the Tatra Mountains, Central Western Carpathians: Tectonometamorphic records of Variscan and Alpine Orogeny. *Geolines, 13*, 141-148.

Kohút, M., & Janák, M. (1994). Granitoids of the Tatra Mts., Western Carpathians: Field relations and petrogenetic implications. *Geologica Carpathica, 45(5)*, 301-311.

Lavaure, S., & Sawyer, E. W. (2011). Source of biotite in the Wuluma Pluton: Replacement of ferromagnesian phases and disaggregation of enclaves and schlieren. *Lithos, 125*, 757-780. DOI: 10.1016/j.lithos.2011.04.005.

Moussallam, Y., Schneider, D. A., Janák, M., Thoni, M., & Holm, D. K. (2012). Heterogeneous extrusion and exhumation of deep-crustal Variscan assembly: Geochronology of the Western Tarta Mountains, northen Slovakia. *Lithos, 144-145*, 88-108. DOI: 10.1016/j.lithos.2012.03.025.

Müller, A., van den Kerhof, A. M., & Broekmans, M. A. T. M. (2011). Trace element content and optical cathodoluminescence of kyanite. *X International Congress for Applied Mineralogy, Trondheim*, 453-461. DOI: 10.1007/978-3-642-27682-8_54.

Olsen, S. N. (1984). Mass-balance and mass-transfer in migmatites from the Colorado Front Range. *Contribution to Mineralogy and Petrology, 85*, 30-44.

Pearson, G. R., & Shaw, D. M. (1960). Trace elements in kyanite, sillimanite and andalusite. *American Mineralogist, 45*, 808-817.

Pyka, P., Szopa, K., Gawęda, A., & Krzykawski, T. (2013a). Kyanite-quartz segregations in the metamorphic complex of the Western Tatra Mountains, Central Western Carpathians. *In: Broska, I., & Tomašových, A. (Eds.): GEEWEC 2013. Geological evolution of the Western Carpathians: new ideas in the field of inter-regional correlations. Abstract book. Bratislava: Geological Institute, Slovak Academy of Science.*

Pyka, P., Szopa, K., & Gawęda, A. (2013b). Megacrysts of kyanite from Baranèc Mt., Western Tatra Mountains, Slovakia. *Mineralogia, 44 (1-2)*, 35-41. DOI: 10.2478/mipo-2013-0002.

Ruggieri, G., Dallai, L., Nardini, I., Henriquez, E. I., & Arias, A. (2010). Thermo-chemical variatons of the hydrothermal fuids in the Berlin Geothermal Field (El Salvador). *World Geothermal Congress Proceedin, Bali, Indonesia,* 1-7.

Spear, F. S. (1993). *Metamorphic Phase Equilibria and Pressure- temperature- time paths* (ed. 1). Waszyngton: MSA Monograph.

Sun, S. S., & McDonough, W. F. (1989). Chemical and isotopic systematics of oceanic basalts: implications for mantle composition and processes. In Magmatism in the Ocean Basins. Saunders, A. D. and Norry, M. J. (Editors), *Geological Society of London, 42,* 313-345. DOI: 10.1144/GSL.SP.1989.042.01.19.

Taylor, S. R., & McLennan, S. M. (1981). The composition and evolution of the continental crust–Rare Earth Element evidence from sedimentary rocks. *Philosophical Transactions of the Royal Society of London, 301*(1461), 381-399.

Whitney, D. L. (2002). Coexisting andalusite, kyanite and sillimanite: Sequential formation of three Al_2SiO_5 polymorphs during progressive metamorphism near the triple point, Sivrihisar, Turkey. *American Mineralogist, 87*, 405-416.

Widmer, T., &, Thompson, A. B. (2001). Local origin of high pressure vein material in eclogite facies rocks of the Zermatt-Saas Zone, Switzerland. *American Journal of Science, 301*, 627-656.

Yardley, B. W. D. (1989). *An introduction to metamorphic petrology* (1st edition); Longman Scientific & Technical.